Chemical versus mechanical denudation in meta-clastic and carbonate bedrock catchments on Crete, Greece, and mechanisms for steep and high carbonate topography

Richard F. Ott[1*], Sean F. Gallen[2], Jeremy K. Caves Rugenstein[1,a], Susan Ivy-Ochs[3], David Helman[4,5], Charalampos Fassoulas[6] , Christof Vockenhuber[3], Marcus Christl[3], Sean D. Willett[1]

[1]Department of Earth Sciences, ETH Zurich, Zurich, Switzerland

[2]Department of Geosciences, Colorado State University, Fort Collins, US

[3]Laboratory of Ion Beam Physics, Department of Physics, ETH Zurich, Zurich, Switzerland

[4]Department of Soil and Water Sciences, The Robert H. Smith Faculty of Agriculture, Food and Environment, The Hebrew University of Jerusalem, Rehovot, Israel

[5]The Advanced School for Environmental Studies, The Hebrew University of Jerusalem, Jerusalem, Israel

[6]National History Museum of Crete, University of Heraklion, Heraklion, Greece

[a]Now at: Max Planck Institute for Meteorology, Hamburg, Germany

*corresponding author: Richard F. Ott, richard.ott1900@gmail.com

This is a non-peer reviewed preprint submitted to EarthArXiv and has been submitted to *Journal of Geophysical Research: Earth Surface.*

ABSTRACT

On Crete — as is common elsewhere in the Mediterranean — carbonate massifs form high mountain ranges whereas topography is lower in areas with meta-clastic rocks. This observation suggests that differences in denudational processes between carbonate-rich rocks and quartzofeldspathic units impart a fundamental control on landscape evolution. Here we present new cosmogenic basin-average denudation rate measurements from both ^{10}Be and ^{36}Cl in meta-clastic and carbonate bedrock catchments, respectively, to assess relationships between denudation rates, processes, and topographic form. We compare total denudation rates to dissolution rates calculated from 49 new and previously published water samples. Basin-average denudation rates of meta-clastic and carbonate catchments are similar, with mean values of ~ 0.10 mm/a and ~ 0.13 mm/a, respectively. The contribution of dissolution to total denudation rate was < 10% in the one measured meta-clastic catchment, and ~ 40% for carbonate catchments (~ 0.05 mm/a), suggesting the dominance of physical over chemical weathering at the catchment scale in both rock types. Water mass-balance calculations for three carbonate catchments suggests 40-90% of surface runoff is lost to groundwater. To explore the impact of dissolution and infiltration to groundwater on relief, we develop a numerical model for carbonate denudation. We find that dissolution modifies the river profile channel steepness, and, together with infiltration changes, the fluvial response time to external forcing. Furthermore, we show that infiltration of surface runoff to groundwater in karst regions is an efficient way to steepen topography and generate the dramatic relief in carbonates observed throughout Crete and the Mediterranean.

1 INTRODUCTION

In many regions, carbonates form high cliffs and topography in comparison with other sedimentary and sometimes magmatic and metamorphic rocks (Atkinson & Smith, 1976). This observation is ubiquitous throughout the Mediterranean (Godard et al., 2016). For example, on the island of Crete, the landscape is dominated by high and steep carbonate massifs that define the backbone of the island, whereas areas underlain by silica-rich metamorphic units exhibit lower topography and gentler slopes (Fig.1). While to the prominent topographic expression of carbonate bedrock in the Mediterranean is ubiquitous, the reasons for high carbonate topography remain poorly understood, primarily because of the lack of quantification of the processes acting to denude carbonates.

Karstic terrains are often interpreted as landscapes where chemical dissolution dominates over physical erosion (Frumkin, 2013); this paradigm has survived many decades without quantitative testing. The importance of dissolution on the weathering of limestones was recognized as early as the late 18th century (Hutton, 1795) and studies of dissolution rates in limestones have been carried out since the 19th century (Goodchild, 1890; Spring & Prost, 1884). Today, dissolution rate calculations from dissolved loads in rivers and springs are routine (e.g. (Gaillardet, Calmels, Romero-Mujalli, Zakharova, & Hartmann, 2018; Gombert, 2002; Gunn, 1981; Meybeck, 1987); however, the quantification of mechanical rock removal from the same area has proven difficult , except for certain cave systems (Newson, 1971). With the development of cosmogenic nuclide techniques, a tool is available to quantify total denudation, and thus mechanical rock removal when the chemical weathering component is known.

Stone, Allan, Fifield, Evans, and Chivas (1994) first established the use of the ^{36}Cl cosmogenic nuclide to determine bedrock denudation rates in limestones. Previous studies of ^{36}Cl denudation rates have focused on exposed bedrock denudation rates, where dissolution is the

dominant lowering process (Godard et al., 2016; Schaller et al., 2005; Thomas et al., 2018; Xu et al., 2013). However, quantification of carbonate denudation at the catchment scale is needed to integrate the effects of mechanical denudation processes along hillslopes and channels and to understand its impact on relief generation. Ryb et al. (2014) were the first to compare dissolution rates with bedrock and catchment average denudation rates from cosmogenic nuclides in carbonate catchments. They found that in Israel dissolution rates were lower than ^{36}Cl-derived denudation rates and suggested that this discrepancy was due to higher precipitation rates, and thus higher dissolution rates, in the past. These authors argue that the effects of past, higher dissolution rates are incorporated into the cosmogenic nuclide concentrations that integrate millennial timescales but not chemical dissolution rates derived from water that integrate a much shorter time.

The elevated role of dissolution in denudation of carbonates relative to other rock types is related to the development of karst features and landscapes. Karst development alters hydrology by increasing water infiltration and decreasing surface discharge to river systems, which affects denudational processes. We hypothesize that the partitioning of dissolution and mechanical weathering in carbonates scales differently with slope and relief compared to other lithologies and will, therefore, exhibit different topographic responses to external forcings, such as climate and tectonics. Moreover, several studies have suggested that dissolution can affect the shape of cave stream profiles (Covington, Prelovšek, & Gabrovšek, 2013; Springer, Wohl, Foster, & Boyer, 2003; Woodside, Peterson, & Dogwiler, 2015), however we have limited understanding of how altitude-dependent changes in dissolution rate influence river longitudinal profiles in carbonate settings (Covington et al., 2013).

In this study, we address these knowledge gaps by measuring total denudation, dissolution rate and water mass balance at the catchment scale in carbonates and meta-clastic Phyllite and Quartzite units (PQ) on Crete and construct river profile models to assess the dominant factors (e.g. physical and chemical denudation, and subsurface water infiltration) contributing to elevated and steep carbonate terrain compared to quartz-rich rocks in the Mediterranean. To partition total denudation between chemical and mechanical weathering in karst landscapes, we analyze seven ^{36}Cl samples of detrital carbonate sands from Crete and 49 water samples from published and new data (Fig.1). To test how substrate erodibility might contribute to differences in topography and relief between carbonates and other lithologies, we determined denudation rates from 16 ^{10}Be detrital samples in the PQ unit and assessed the partitioning between chemical and mechanical weathering in this unit with an approach similar to the karst areas. We use a numerical model of carbonate denudation to explore the effects of carbonate denudation processes and hydrology on the generation of topography. We explore how the infiltration of runoff to groundwater in limestone karst areas and dissolution change the relief and the shape of river profiles and how climatic and tectonic conditions influence carbonate topography.

2 BACKGROUND

The island of Crete occupies a forearc high above the Hellenic subduction zone, a long-lived system in which Africa is presently subducting below Eurasia at ~ 36 mm/a (Reilinger et al., 2006). From the Cretaceous to the early Miocene, subduction of continental slivers or attenuated crustal lithosphere and oceanic domains resulted in a thick nappe pile (van Hinsbergen et al., 2005). The Permian to Oligocene Plattenkalk and Jurassic Trypalion carbonate

115 units were underthrusted below the Carboniferous to Middle Triassic PQ unit, and all units
116 underwent high pressure – low temperature (HP-LT) metamorphism (Fassoulas, Kilias, &
117 Mountrakis, 1994; Seidel, Kreuzer, & Harre, 1982; van Hinsbergen et al., 2005). These nappes
118 were exhumed by subsequent extension during the Neogene and now unmetamorphosed, Pindos
119 and Tripolitza carbonate units are juxtaposed against HP-LT metamorphic rocks of the Phyillite
120 – Quartzite (PQ) and Plattenkalk units (Rahl, Anderson, Brandon, & Fassoulas, 2005; van
121 Hinsbergen & Meulenkamp, 2006). Miocene to recent multidirectional extension has created
122 numerous sedimentary basins filled with marine and terrestrial deposits (Peterek & Schwarze,
123 2004; van Hinsbergen & Meulenkamp, 2006; Zachariasse, van Hinsbergen, & Fortuin, 2008).
124 Arc normal and parallel extension of the upper crust is ongoing, as evidenced by active normal
125 faults bounding some of the mountain ranges on Crete (Caputo et al., 2010; Gallen et al., 2014).
126 The PQ and carbonate units on Crete are from various positions within the former nappe
127 pile, and there is no clear relationship between stratigraphic position in the former nappe pile and
128 modern elevation in the landscape. Carbonate massifs on Crete reach 2500 m and are
129 characterized by steep flanks with high relief that bound internal areas of lower relief (Fig. 2a).
130 The three main massifs (Lefka Ori, Psiloritis and Dikti) contain several internally drained basins
131 and also have areas that are nearly vegetation free, comprised of natural vegetation of semi-shrub
132 deserts (Fig. 2a) (Bohn & Gollub, 2000). Areas underlain by the PQ bedrock form mountainous
133 landscapes but with elevations generally below 1000 m and are more densely vegetated with
134 olive, kermes oak-mastic and pine forest (Fig. 2b) (Bohn & Gollub, 2000).
135
136 **3 METHODS**
137 **3.1 Cosmogenic nuclide denudation rates**

To compare denudation rates in silicic and carbonate bedrock, we collected quartz- and carbonate-rich fluvial sands to measure ^{10}Be and ^{36}Cl concentrations, respectively, using Accelerator Mass Spectrometry (AMS) at ETH Zurich. Samples for ^{10}Be were gathered from rivers draining the meta-clastic PQ unit that is mainly exposed in western Crete. We collected ^{36}Cl samples from carbonate catchments spanning a wide range of elevations and relief to see if denudation scales with topographic metrics, which would imply a contribution of mechanical denudation.

3.1.1 Detrital ^{10}Be denudation rates

We collected 16 samples of fluvial sands with grain size 0.25 - 0.71 mm for ^{10}Be analysis. All sampled catchments lie within the meta-clastic PQ unit. Most sampled catchments are underlain almost entirely by the PQ unit, except samples WC-616-11 and WC-616-16 where other rock types, such as carbonate and flysch, span ~40% of the catchment. We separated quartz from the bulk sediment by magnetic separation and repeated etching in hydroflourosilicic and diluted hydrofluoric acid. A ^{9}Be carrier was added before dissolving the quartz with hydrofluoric acid. Beryllium was extracted using standard column chromatography (Bierman et al., 2002). The ^{10}Be/^{9}Be isotope ratio was measured by 500kV TANDY at ETH Zürich and calibrated using S2007 N ^{10}Be standard (Christl et al., 2013). Blank corrected ^{10}Be concentrations were used to calculate erosion rates based on the equations from Brown, Stallard, Larsen, Raisbeck, and Yiou (1995) (detailed AMS data in Tab. S5). Production rates were calculated in a pixel-based approach with the scaling scheme of Stone (2000), assuming a rock density of 2.7 g/cm^3 and attenuation lengths for neutrons, slow and fast muons from Braucher, Merchel, Borgomano, and Bourlès (2011) on a 30 m SRTM elevation model, averaged for every catchment and corrected

for topographic shielding. Denudation uncertainties include analytical uncertainty and 2.5%, 50% for the production uncertainties of neutrons and muons, respectively (Lupker et al., 2012).

3.1.2 Detrital ^{36}Cl denudation rates

Seven samples of fluvial sediments with grain size 1 – 4 mm were collected for catchment average denudation rates in areas dominated by carbonates using ^{36}Cl. We sampled catchments within the Plattenkalk, Trypalion, and Pindos units. The grain size, which is larger than that used for ^{10}Be, was chosen to avoid aeolian material transported by strong coastal winds in some catchments and to be able to sample small steep catchments lacking sand size river sediments. The samples were crushed to grain size < 0.5 mm. Meteoric ^{36}Cl was removed by etching with 2 M HNO_3 and repeated rinsing. A ^{35}Cl- enriched spike (Ivy-Ochs, Synal, Roth, & Schaller, 2004) was added, and the samples were dissolved with HNO_3 (Prager, Ivy-Ochs, Ostermann, Synal, & Patzelt, 2009). Measurements of ^{36}Cl were conducted at the Laboratory of Ion Beam Physics 6 MV TANDEM AMS system at ETH-Zürich using a gas-filled magnet to separate the isobar ^{36}S (Vockenhuber, Miltenberger, & Synal, 2019) and calibrated with the internal K382/4N standard (Christl et al., 2013). The AMS data with and without blank correction are shown in the supplementary table S6. The chemical composition of the target and the bulk rock was determined by separate ICP-MS analysis of the bulk sample and the undissolved sample remnant (if not all the material dissolved). The chemical composition of the bulk samples and target used for calculation is reported in the supplement (Tab. S4).

^{36}Cl concentrations and carbonate chemistry were used to calculate denudation rates following the approach of Schimmelpfennig et al. (2009) with the scaling by Stone (2000) and a topographic shielding correction. The scaling factors of nucleonic and muonic production were calculated with CRONUS (Marrero et al., 2016) using the mean basin latitude and altitude

183 calculated by a pixel-based approach on a 30m SRTM digital elevation model. The
184 Schimmelpfennig et al. (2009) denudation rate calculation does not include an uncertainty
185 propagation. However, the current version of CRONUS is incapable of calculating erosion rates
186 and uncertainties for low concentration ^{36}Cl samples. Therefore, we used the relative error for
187 our samples calculated with a reference total nuclide concentration of $4e^5$ at/g (close to the mean
188 of our measured concentrations) and ensured that the effect of total nuclide variation on the
189 expected relative error is negligible. The samples were run in CRONUS with this reference
190 nuclide concentration while all other sample specific input parameters (nuclide concentration
191 uncertainty, sample chemistry) were adjusted. This approach allowed us to incorporate the
192 analytical uncertainty from the AMS measurement and Cl-concentration as well as the
193 production rate uncertainties. Additional uncertainties incorporated for pressure, sample
194 thickness, bulk density and effective attenuation length are 10 hPa, 0.01 cm, 0.1 g/cm³ and 10
195 g/cm², respectively.

196 **3.2 Dissolution rates**

197 ***3.2.1 Water sample collection and analysis***

198 We collected a set of seven water samples from springs, rivers, and Lake Kournas. We
199 used our data in conjunction with 42 water samples from springs, wells, rivers and lakes from
200 Crete, collected by the National Water Monitoring Network, Greece and compiled from
201 Papaioannou (2007) and Kallianis and Chatzitheodorou (2003) (Tab. S1). We collected two
202 samples per site for cations and anions in HDPE bottles and filtered samples on-site through a
203 0.2 μm filter. Alkalinity was measured in the field with a sulfuric acid titrant and a bromcresol
204 green - methyl red indicator. Cation samples were acidified, and anion samples kept refrigerated
205 until measurement. To gauge the source altitude of water samples, we measured $\delta^{18}O$ on each

sample. See supplement for details about ion concentration and $\delta^{18}O$ measurements. Cation and anion concentrations were corrected for precipitation input by using the lowest [Cl^-] measurement from the Zaros spring, which is sourced by meteoric water from the high-elevation (> 1000 m), evaporite-free Psiloritis Mountains and assuming all [Cl^-] is precipitation derived. The other ions were then corrected by scaling with seawater ratios (Stallard & Edmond, 1981).

3.2.2 Dissolution rate calculation

We use a trimonthly, three year time series from seven sites collected by the National Water Monitoring Network, Greece (Tab. S1) to assess chemostatic behavior (Godsey, Kirchner, & Clow, 2009) (*i.e.*, constant chemical concentrations even as discharge varies) of the respective water source (Fig. 3). Variations of [Ca^{2+}] are < 10% and [Mg^{2+}] < 20% throughout the year; therefore, we assume chemostatic behavior of the cations and anions for our analysis. Time-averaged concentrations of Ca^{2+} and Mg^{2+} (in mg/l) are used to calculate average carbonate dissolution rates D (in mm/a) with the following equation:

$$(1)\ D = \frac{\left([Ca] + \frac{[Ca]}{M_{Ca}} * M_{CO_3}\right) * (P - AET)}{\rho_{Calcite} * 10^6} + \frac{\left([Mg] + \frac{[Mg]}{M_{Mg}} * M_{CO_3}\right) * (P - AET)}{\rho_{Dolomite} * 10^6}$$

Where precipitation (P) and actual evapotranspiration (AET) are in mm/a and the densities (ρ) in g/cm^3. M_{Ca}, M_{Mg}, and M_{CO3} are the molar masses of the respective ions. The factor 10^6 converts the dissolution rate into units of mm/a. This calculation assumes dissolution mainly at or close to the surface, an assumption verified by Gunn (1981). Saturation indices are calculated in PHREEQC (Parkhurst & Appelo, 1999) assuming chemical equilibrium.

Information on the potential discharge (Q_{pot} = P - AET) available for dissolution is required to determine the amount of total dissolution. To calculate Q_{pot}, we used the average monthly P data provided by WorldClim at 1 km spatial resolution (Fick & Hijmans, 2017),

228 which was averaged for the catchment area of the water sample. We used annual estimates of
229 AET derived from the Parameterization of Vegetation Indices for Evapotranspiration (PaVI-E)
230 model (Helman, Givati, & Lensky, 2015). The PaVI-E model uses spectral vegetation indices
231 from the MODerate resolution Imaging Spectroradiometer (MODIS) onboard the Terra satellite
232 and information on water vapor flux from the eddy covariance tower international net
233 (FLUXNET) to derive empirically annual AET from 2000 to 2016 at 1 km spatial resolution (a
234 detailed description of the estimation of AET is in the supplement). Analogous to P, AET was
235 averaged for each catchment. Finally, Q_{pot} was calculated at 1 km resolution from P and AET.
236 Groundwater recharge areas were estimated from topography and local geology (Fig. S1). These
237 areas were used to calculate Q_{pot} for springs and aquifer samples, while surface water catchment
238 areas were used to calculate Q_{pot} for surface water samples.
239 However, recharge areas of karst aquifers commonly differ from their topographic
240 delineation (e.g. Malard, Sinreich, and Jeannin, 2016); therefore we applied a 10% uncertainty
241 on P and 20% uncertainty on AET (together with the 5% analytical uncertainty of the reported
242 concentrations). To further test the reliability of the water fluxes incorporated into the dissolution
243 rates we also calculated dissolution rates based on (1) the mean P and AET on all Cretan
244 carbonate areas between 23.8 and 25.8° longitude and (2) the mean P and AET for every
245 carbonate massif separately from, which our samples are recharged (Tab. S1). To assess the
246 contribution of chemical weathering in meta-clastic catchments, we calculated the chemical rock
247 removal by dissolution for the Topolia catchment (location in Fig. 4a). From this water sample,
248 we calculated the total dissolved flux from this catchment and compared it to the total flux
249 predicted by the ^{10}Be measurement at the same location.

250 **3.3 Numerical modelling of carbonate denudation**

To test the effect of different denudation processes acting in carbonate landscapes, we use a 1D numerical model of topographic evolution. The model domain is uplifted at a uniform rate (U = 0.2 mm/a), and denudation is calculated with two separate process rules - mechanical erosion (E) and dissolution (D) to simulate chemical weathering rate. The rate of surface elevation change can then be described as:

$$(2)\ \frac{dz}{dt} = U - E - D$$

E can be described by the detachment-limited stream power model,

$$(3)\ E = K * {Q_{pot}}^{m} * S^{n},$$

where K is a coefficient incorporating erodibility of the substrate, climate, and hydrology, Q_{pot} is the potential discharge (P – AET), and S is the local channel slope. m and n are empirical constants depending on basin hydrology, channel geometry and erosion process (Whipple & Tucker, 1999). We use the common values of n = 1 and m = 0.5 for our numerical models (Whipple, Hancock, & Anderson, 2000).

Assuming that runoff rapidly reaches saturation, limited by temperature and pCO_2, the mass loss can be expressed as a surface lowering rate due to dissolution (in mm/a) after White (1984) as

$$(4)\ D = \frac{1}{\rho 10\sqrt[3]{4}} * \left(\frac{K_c K_1 K_{CO_2}}{K_2}\right)^{\frac{1}{3}} {pCO_2}^{1/3} * (P - AET)$$

where ρ is the density of limestone (in g/cm³), K_c, K_1,K_2 and K_{CO2} are the equilibrium constants of the calcite-CO_2-H_2O system and P and AET are in mm/a (not to be confused with K, the erodibility parameter). The change of surface elevation can then be described as:

$$(5)\ \frac{dz}{dt} = U - K(Q_{pot}(z) * I)^m S^n - \frac{1}{\rho 10\sqrt[3]{4}} * \left(\frac{K_c(z)K_1(z)K_{CO_2}(z)}{K_2(z)}\right)^{\frac{1}{3}} pCO_2(z)^{\frac{1}{3}}$$

$$* \left(P(z) - AET(z)\right)$$

We introduce the infiltration parameter (I) to the stream power portion of the equation to analyze the infiltration of runoff to groundwater ($I = \frac{Q}{Q_{pot}}$), as commonly observed in karst landscapes. To quantify the magnitude of infiltration, we calculated water budgets for three catchments on Crete from the P, AET, and gauging data (see Table S2).

In the case of a steady-state ($\frac{dz}{dt} = 0$), equations (2) and (3) can be combined and solved for the steady-state local channel slope S and the infiltration parameter can be added:

$$(6)\ S = \left(\frac{U - D}{K}\right)^{1/n} * (Q_{pot} * I)^{-\frac{m}{n}}$$

The form of this equation is the same as Flint's (1974) law:

$$(7)\ S = k_s * Q^{-\frac{m}{n}}$$

where k_s is the steepness index. As such $k_s = \left(\frac{U-D}{K}\right)^{\frac{1}{n}}$. In similar expressions that exclude the dissolution term in equation 2, the first term in equation 6 takes on the form $\left(\frac{U}{K}\right)^{\frac{1}{n}}$ and many researchers have used the relationship between k_s values to infer tectonic signals from topography. Following these previous studies, we refer to the first term on the right-hand side of equation 6 as the dissolution steepness index, k_{sd}.

4 RESULTS

4.1 Cosmogenic denudation rates

4.1.1 Denudation rates and patterns

Denudation rates derived from ^{10}Be in meta-clastic catchments range from 0.048 to 0.26 mm/a with a mean of 0.1 mm/a (Tab. 1), which are lower than late Pleistocene coastal uplift rates (0.2 – 1 mm/a) (Gallen et al., 2014; Ott et al., 2019) (Fig. 4). The denudation rates show no obvious spatial pattern among the meta-clastic PQ unit (Fig. 4). ^{36}Cl-derived catchment-averaged denudation rates from carbonate sands in limestone dominated catchments range from 0.052 – 0.56 mm/a (Tab. 1, Fig. 4). The highest value of 0.56 mm/a is in the Samaria Gorge, one of Europe's deepest gorges with ~ 2 km of relief (Fig. 4a). The next highest denudation rate is 0.18 mm/a from a similar gorge nearby. The low concentrations measured for the Samaria Gorge represent an outlier in our dataset, which is not unexpected. The Samaria gorge has vertical walls of several hundreds of meters that are prone to rockfall and landsliding; therefore, a contribution of rockfall or landslide material may explain the low ^{36}Cl concentration, and we consequently removed this data point from our analysis. Carbonate denudation rates along the high mountain ranges are slightly elevated compared to denudation rates in meta-clastic catchments (Fig. 4a, b). Carbonate denudation rates along the lower relief topography of northeastern Crete are similar to the rates from western Crete (Fig. 4c). Generally, the denudation rates in the carbonate catchments are similar to the rates in meta-clastic catchments but are slightly higher in areas of steep and high topography (Fig. 4a, b).

4.1.2 Correlation between denudation rates and topographic/climatic metrics

We compare our denudation rates with topographic and climatic metrics for each catchment (Fig. 5). We use a correlation coefficient matrix to assess the strength of parameter relationships within the dataset (Fig. 5g). The correlations between denudation rate and other catchment metrics within the ^{10}Be dataset are generally weak ($r^2 < 0.4$) (Fig. 5 a-f). However, the meta-clastic catchments exhibit similar topography and erosion rates and thus do not span

enough range to assess correlations adequately (Fig. 5). Carbonate catchments, in contrast, cover a larger topographic and climatic gradient than meta-clastic catchments and exhibit stronger correlations of denudation rates with several topographic metrics as well as precipitation (Fig. 5). The correlation coefficient matrix shows the same pattern, with weaker correlations in meta-clastic catchments and stronger correlations ($r^2 > 0.5 \mid r^2 < -0.5$) in carbonate catchments (Fig. 5g). For example, in carbonate catchments, the mean catchment elevation scales inversely with AET (Fig. 5g), likely due to decreasing vegetation cover and consequently of plant transpiration (usually the main component in AET) at higher elevations. The effect of orographic precipitation is noted by the correlation of precipitation with mean elevation and total relief (Fig. 5g). P-values for correlation significance are sample size dependent, an effect manifested in the small ^{36}Cl dataset (n = 7) that shows some p-values that are higher than in the larger ^{10}Be dataset (n = 16) (Tab. S7). However, the p-values for correlations between topographic metrics and denudation rate in the ^{36}Cl catchments are lower compared to ^{10}Be catchments, and as such the correlation between ^{36}Cl denudation rate and local relief is still significant at a 90% level (Tab. S7).

In summary, the good correlations between denudation rate and topographic metrics in carbonate catchments likely imply a causal relationship between topography and denudation. The available data in meta-clastic catchments span too narrow a range to assess mutual relationships between denudation rates and topographic metrics adequately.

4.2 Water chemistry and dissolution rates

The chemical signature of Cretan water samples varies among the different water sources (Fig. 6). Water samples from carbonate catchments have a mean $[Ca^{2+}]$ of 63 mg/l and a mean $[Mg^{2+}]$ of 20 mg/l. River water has higher $[Ca^{2+}]$ and $[Mg^{2+}]$ compared to subsurface water from wells and springs. Groundwater samples also have less variability in their concentrations. The

337 values of pCO_2 also vary by water source. Most river samples were oversaturated and we also
338 calculate the pCO_2 at which they would have been in equilibrium (Fig. 6c). The pCO_2 for spring
339 and groundwater are higher as for river water.If we take into account potential degassing of CO_2
340 in river water and calculate the pCO_2 at which the river water would have been in equilibrium,
341 this relationship is reversed (Fig. 6c), however these theoretical pCO_2 should not be taken at face
342 value becacuse the Sr/Ca ratios of > 2 (ppb/ppm) indicate likely secondary carbonate
343 precipitation (Bickle, Tipper, Galy, Chapman, & Harris, 2015) (Tab. S1). The values for $[Na^+]$,
344 $[SO_4^{2-}]$ and $[Cl^-]$ vary widely between different catchments and are potentially related to small
345 amounts of evaporites in certain catchments (Tab. S1). We focus our analysis on $[Ca^{2+}]$ and
346 $[Mg^{2+}]$ because we are mostly interested in the rates of carbonate dissolution.
347 $[Ca^{2+}]$ and $[Mg^{2+}]$ vary not only with water source but also with catchment elevation (Fig.
348 7). $[Ca^{2+}]$ decreases with elevation of the recharge area, as does the saturation index with respect
349 to calcite (Fig. 7a). Crete displays a clear increase of precipitation with elevation due to
350 orography and a simultaneous decrease in evapotranspiration (Fig. 5). In terms of $[Ca^{2+}]$ fluxes
351 or dissolution rates, there is little change with elevation because the reduced concentrations at
352 high altitude are offset by increased water flux due to the coupled effects of increased
353 precipitation due to orography and reduced evapotranspiration at higher elevations on Crete (Fig.
354 7c). A matrix of all correlation coefficients (analogous to Figure 5g) for our water sample data is
355 available in the supplement (Fig. S2). Our calculated carbonate dissolution rates vary between
356 0.016 and 0.150 mm/a, with a mean of 0.048 ± 0.011 mm/a. The different methods to estimate
357 water fluxes for dissolution described in the methods produced overall similar results with some
358 variations in individual catchments but an overall mean dissolution rate of ~ 0.05 mm/a (Tab.
359 S1). To assess the chemical weathering component in the meta-clastic PQ unit we compared the

360 total denudational flux from ^{10}Be to the total dissolved load in the Topolia catchment (Tab.2).
361 We found that < 10% of the denudational flux is from chemical weathering, comparable to other
362 siliciclastic catchments (Dixon & Blanckenburg, 2012).

363 **4.3 Water budgets**

364 For three Cretan catchments with long-duration gauging data, we calculated annual water
365 budgets spanning years 1996 – 2003 for two catchments and 1996 – 2001 for the other basin and
366 determined the approximate ratio of surface to subsurface runoff for each year in each catchment
367 (Tab. S2). We found that on average, 40 to 90% of the potential runoff left the catchments as
368 subsurface flow. The two catchments with lower loss rates of 40 and 57% are in mixed
369 lithologies, whereas the 90% loss rate is from a carbonate-dominated catchment. We lack water
370 budgets for meta-clastic catchments; however, we assume subsurface water flow to be minor
371 similar to other regions underlain by metamorphic rocks (Driscoll, 1987). Since we do not have
372 detailed information about springs and their discharges downstream and upstream of sampling
373 points that could modify the water budgets, these results are subject to considerable
374 uncertainties. However, the finding of large amounts of subsurface flow in the highly karstified
375 Cretan landscape is not surprising, given the occurrence of multiple dry valleys, poljes, and large
376 aquifers. Based on these findings, we use an infiltration of 70% (I = 0.3) of potential discharge as
377 input for our carbonate denudation models in section 5.3.2. It is important to note that the high
378 uncertainties associated with this estimate of I do not influence any of our main conclusions.
379 Below 500 m we use a linear decrease from 70 to 0% infiltration loss, mimicking the increase of
380 infiltration as the topography rises higher above the karst water table. The karst water table
381 below the Lefka Ori carbonate massif on Crete, for example, has been shown to be more than 1
382 km below the land surface in some locations (Nikolaidis, Bouraoui, & Bidoglio, 2013).

5 ANALYSIS AND MODELLING

This study presents an analysis of water and cosmogenic samples from Crete to quantify the mechanical and chemical components to total denudation and relief production in meta-clastic and carbonate catchments. We will first discuss the processes that influence altitude-dependent dissolution rates and how we can use dissolution rates together with the total denudation rates in the carbonate and meta-clastic catchments to quantify catchment-scale chemical and mechanical weathering. We then use numerical simulations to assess the primary factors controlling the various topographic expressions of carbonate and meta-clastic bedrock catchments assuming that carbonate denudation occurs by both mechanical erosion and chemical weathering, while silicic-clastic units erode mostly through mechanical erosion. Simulations were then used to predict the response of carbonate catchments to different forcings.

5.1 Processes controlling water composition of carbonate catchments on Crete

We observed higher [Ca^{2+}] and [Mg^{2+}] surface water concentrations compared to water traveling via the subsurface (Fig. 6). These differences could be related to changes in the CO_2 availability for dissolution. Soil CO_2 concentration is typically an order of magnitude higher than atmospheric values (Brook & Box, 1984), and thus offers an important source of carbonic acid for carbonate dissolution. Soil CO_2 concentrations scale with primary productivity, particularly in semi-arid environments (Cotton & Sheldon, 2012), which typically decreases with increasing elevation (Daubenmire, 1943; Humboldt, 1806). In Crete, natural vegetation varies from forests dominated by olive trees at sea level to pine and cypress-dominated woodlands at intermediate altitudes, and grasslands or barren land at high elevations (Bohn & Gollub, 2000). The origin of the water sampled from groundwater aquifers and springs are the high elevation mountain

406 ranges, as evidenced by more negative $\delta^{18}O$ values similar to the high elevation water samples
407 (Tab. S1). At the top of these mountains, vegetation is quite sparse with mostly barren lands with
408 patches of thin soil (Fig. 2a). Therefore, CO_2 availability for dissolution is mostly restricted to
409 atmospheric CO_2 (and not soil CO_2). Water in streams may represent a mixture between such
410 high elevation low [Ca^{2+}] water and water sourced from lower elevations where more CO_2 for
411 dissolution is available. This interpretation is further supported by the high pCO_2 – typical for
412 soil systems- at which the supersaturated water samples would be in equilibrium (Fig. 6c).
413 However, pCO_2 values for the rivers are difficult to interpret due to supersaturation suggesting
414 CO_2 degassing and Sr/Ca (ppb/ppm) ratios > 2 indicative of secondary carbonate precipitation
415 (Bickle et al., 2015).
416 Calcite solubility increases with decreasing temperature (Plummer & Busenberg, 1982)
417 and therefore, the potential for dissolution should increase with elevation if all other parameters
418 are held constant. However, the aforementioned processes override the effect of a general calcite
419 solubility increase with lower temperatures. Decreases of [Ca^{2+}] with altitude due to a decrease
420 in soil CO_2 have also been observed in river and spring water in Swiss Jura mountains (Calmels,
421 Gaillardet, & François, 2014) and limestone dissolution tablet measurements in the Alps (Plan,
422 2005). However, the runoff available for dissolution increases due to orographic rainfall and
423 lower evapotranspiration rates at high altitudes. On Crete, this effect almost balances the
424 decrease of [Ca^{2+}] and leads to a less pronounced decrease in the carbonate dissolution rate with
425 altitude (Fig. 7c).
426

427 **5.2 Chemical versus mechanical denudation in carbonates and clastics**

Our calculation of total dissolved loads in the Topolia meta-clastic catchment (Tab. 2) showed that < 10% of the total denudational flux in this catchment is through the dissolved load. This result is supported by Gaillardet, Dupré, Louvat, and Allègre (1999) and Larsen et al. (2014) who estimated that globally chemical weathering in silicates is responsible for < 5% of the denudation. Therefore, we assume that chemical weathering in the PQ bedrock is minor and that surface lowering is largely achieved by mechanical weathering.

The average calculated dissolution rate for carbonate catchments is ~ 0.05 mm/a (Tab. S1). This rate is nearly a factor of 3 lower than the average carbonate denudation rate of 0.13 mm/a, but implies that dissolution shoulders a greater proportion of denudation in carbonate catchments (~ 40%) compared to the PQ catchment. Figure 8 shows the difference between total denudation rates and dissolution rates on Crete. Denudation rates in carbonate catchments increase with topographic metrics such as local and total relief, normalized channel steepness (k_{sn}) and elevation (Fig. 5g), whereas carbonate dissolution rates do not show this correlation. The correlation of total denudation with topographic metrics indicates that the discrepancy between total denudation rates and dissolution rates is best explained by mechanical erosion in the carbonate catchments.

A previous study by Ryb et al. (2014) explained a similar discrepancy through higher precipitation (MAP) rates in the past. A higher paleo-MAP would result in a higher water flux available for dissolution and thereby increase paleo-dissolution rates. Average catchment erosion rates in our case integrate over a time window of 4 – 6 ka. Tritium concentrations of well and spring data range from 0.7 to 5 tritium units and indicate a mix of submodern (recharged prior to 1952) and modern water for most aquifers (Polychronaki, Pavlidou, & Zouridakis, 2009). Our water samples are snapshots of modern to submodern conditions depending on the water source.

Ryb et al. (2014) observed the same discrepancy between total denudation and dissolution rates and argued that this reflects a higher paleo-MAP, based on the weak correlation of slope with their denudation rates. However, paleo-MAP reconstructions for 6 ka show no relevant difference from modern precipitation rates on Crete (Hijmans, Cameron, Parra, Jones, & Jarvis, 2005). Moreover, our carbonate denudation rates do scale with topographic metrics, whereas a simple increase in paleo-MAP is not expected to cause relief-dependent changes in denudation rates. For these reasons, we suggest carbonate dissolution rates have remained relatively steady over the time-scale integrated by our cosmogenic nuclide derived erosion rates and that the discrepancies between total denudation and dissolution in carbonates primarily reflect the roles of physical weathering and erosion.

The correlation of denudation rates with precipitation and the lack of correlation between dissolution rates and precipitation (Fig. S4) illustrates that increases of carbonate denudation with precipitation are not necessarily the result of increased dissolution due to a higher water flux. Alternatively, discrepancies between erosion and dissolution can be caused by increased mechanical erosion in steep and high landscapes.

5.3 Mechanisms for high carbonate topography and low PQ topography

5.3.1 Erodibility in carbonates and meta-clastic rocks and landscape response

Coastal uplift data from western and southern Crete show that the PQ-unit and the carbonate mountain ranges are often fault bound (Ott et al., 2019; Wegmann, 2008) but that despite similar uplift rates the topographic expression of the carbonate mountains is much higher. Another explanation for higher and steeper carbonate topography is a difference in erodibility (K) between the PQ-unit and the different carbonate units. Under this reasoning, carbonate catchments would have a lower K-value that would require them to steepen to maintain

474 denudation rates similar to those in the meta-clastic catchments (equation 3). However, K
475 incorporates climatic and hydrologic parameters as well as substrate erodibility within the simple
476 stream power framework. On Crete, we do not expect a substantial climatic difference between
477 our catchments, whereas our water budgets imply marked differences in hydrology between
478 meta-clastic and carbonate catchments. The substrate erodibility is relatively challenging to
479 quantify directly, and the carbonates exhibit landforms diagnostic of karst hydrology. We,
480 therefore, choose to assess the impact of hydrologic behavior by incorporating hydrologic
481 parameters into the discharge term Q of equation 5 and explore the effects of infiltration of
482 surface runoff in karst areas on topography. We can use this characterization of infiltration to test
483 if the difference in hydrology between units is sufficient to explain differences in relief or if an
484 additional difference in substrate erodibility is required. Also, the combined action of dissolution
485 and mechanical erosion in the carbonate catchments should scale differently with elevation than
486 denudation in the PQ unit that is dominated by mechanical processes, demonstrating the need to
487 explore plausible mechanisms of relief generation.

488 ***5.3.2 Landscape response to infiltration and dissolution***

489 To explore the landscape response to dissolution and the infiltration of runoff to
490 subsurface flow, we model the evolution of topography over time explicitly accounting for
491 mechanical and dissolution-related denudation as well as the effect of subsurface infiltration. The
492 erodibility parameter K was chosen to be 10^{-5} to mimic the fluvial relief of Cretan mountain river
493 systems. To calculate the portion of denudation due to carbonate dissolution, we scale AET,
494 precipitation, temperature, and soil pCO_2 with altitude. Scaling of AET and precipitation was
495 accomplished by fitting functions to P/AET versus altitude plots for satellite data on Crete within
496 carbonate terrain (Fig. S2). Soil CO_2 was scaled with AET based on the relationship from Brook,

497 Folkoff, and Box (1983). The range of $\log_{10}(pCO_2)$ predicted by the model (-3.05 to -2.40) is
498 similar to the values observed in our water samples (Fig. 6c). Soil CO_2, effective precipitation,
499 and temperature are then used to calculate a carbonate lowering rate with equation (4). We run
500 the model until a steady-state topography is achieved. The empirical equations used, a listing of
501 parameters and a detailed scheme of the model setup are in the supplement (Tab. S3, Fig. S3).
502 Figure 9 shows the steady-state topography of 1D river profiles for different denudation
503 processes in a homogeneously uplifting mountain range (for the transient response see Fig. S5).
504 Precipitation on Crete increases with elevation whereas AET decreases. These trends lead to a
505 strong net increase in runoff with altitude that is available for both dissolution and mechanical
506 river incision (Fig. 9b). The decrease of AET with elevation is linked to a decrease of primary
507 productivity and therefore scales with the production of soil CO_2. Dissolution scales with the
508 cube root of CO_2 but linearly with the availability of water (see EQ. 4). Therefore, dissolution in
509 our model increases with elevation despite a strong decrease in soil CO_2. This increase of
510 carbonate dissolution rate predicted by the model is not observed in our dissolution rates from
511 Crete (Fig. 7c); however we lack water samples from streams at high elevations.
512 The dissolution rates calculated within our model from equation four are landscape
513 averages. Studies by Palmer (1991) and Covington et al. (2013) showed that dissolution rates in
514 cave streams can be higher than these landscape average rates. However, all water samples we
515 collected from local streams were saturated with respect to calcite and therefore would not
516 permit additional dissolution along the stream. In this case, only where undersaturated water
517 from springs or the surroundings enters a stream, can additional dissolution occur. Our model
518 dissolution is a representation of locally adding undersaturated water from the surroundings, but
519 does not include additional dissolution, nor discharge related to potential springs at the base of

carbonate massifs. Hence, we note that there is uncertainty on the dissolution rates along the stream profile which inhibits a direct relation of the modelled magnitude of the dissolution effect to natural stream profiles. However, the uncertainty of in-stream dissolution rates does not affect any of the conceptual conclusions drawn below.

Model runs that include dissolution exhibit lower relief and gentler slopes compared to models with only detachment limited stream power incision (Fig. 9a). The contribution of dissolution to the surface lowering acts to decrease the river gradient because less mechanical erosion is required to balance the uplift. This is in agreement with findings from Springer et al. (2003) who observed this behavior in stream profiles in West Virginia, USA.

The variation of dissolution rate with altitude will also alter the shape of a river profile by changing the dissolution channel steepness index k_{sd} along the profile. While standard detachment limited stream profiles will exhibit a constant channel steepness k_s, altitude dependent dissolution processes will lead to a non-uniform channel steepness k_{sd}. If dissolution is not considered but is important in the longitudinal profile evolution, such variations in steepness might be interpreted as changes in channel concavity. A dissolution rate that increases with altitude, as the one we modelled will lead to a progressive upstream decrease in k_{sd} because an increasing portion of denudation will be through slope-independent dissolution (Fig. 9d). We also used the empirical equation derived from the linear fit to our carbonate dissolution rates with altitude (Fig. 7c). In this model run dissolution decreases with altitude due to infiltration (with a constant value above 1300 m to avoid dissolution rates that reach zero). When the empirical dissolution rate is applied, k_{sd} is lower than in a stream power model (SPM) and the difference reduces with altitude (Fig. 9d).

While dissolution acts to reduce the steepness of river profiles, the opposite occurs when infiltration of surface runoff is included in the model (Fig. 9a). The associated reduction in stream discharge generates a steady-state topography that is higher and steeper by a factor of $I^{-m/n}$ (~ 1.8 in our model) compared to the standard stream power model (based on the integration of equation 7). Equation (1) implies that a decrease in discharge will need to be compensated by an increase of slope to achieve the same erosion rate. Therefore rivers in carbonate catchments that typically experience high amounts of infiltration to the karst system will steepen their gradient to maintain the same denudation rate, consistent with the hypothesis of Gallen and Wegmann (2017) posed for rivers in south-central Crete. The PQ unit is predicted to denude through mechanical processes without substantial infiltration of runoff and therefore are less steep than carbonate catchments to match the same rock uplift. This mechanism provides one possible explanation for the limited range in the values of the topographic metrics observed in the PQ-catchments (Fig. 5).

These results also imply that topography in carbonates will respond differently to changes in uplift rate compared to areas with little subsurface infiltration and without dissolution. The landscape response time is defined by the timescale required for a perturbation (e.g. a change in tectonic or climatic forcing) to propagate from the river outlet to the channel head (Howard, 1994). Infiltration and dissolution will change the original response time equation from Whipple and Tucker (1999) to:

$$(9)\ \tau = \int_0^x \frac{dx}{K * {Q_{pot}}^m * {I_{up}}^m S^{n-1} + D}.$$

Infiltration during the uplift of a limestone mountain range (decreasing I) above the karst water table will increase the time of landscape adjustment. Here, we have modified I to I_{up} to highlight that amount of infiltration loss upstream of the knickpoint sets the response time. This

565 rate of upstream infiltration rate might change as the knickpoint migrates. In a block
566 experiencing a sudden uplift increase without a prior karst network, infiltration rates are likely to
567 increase upstream and will therefore mainly affect the response time of the upper channel
568 reaches. Fabel, Henricksen, Finlayson, and Webb (1996) showed this behavior in an Australian
569 carbonate stream, where the development of karst lead to the abandonment of the stream channel
570 during normal flow conditions and therefore almost stalled the migration of stream knickpoints.
571 In our example model, the response time of a 10 km long mechanically denuding basin (e.g. PQ
572 –unit) is 7.5 Ma. This increases to 13.7 Ma for a carbonate catchment and 11.5 Ma when an
573 increase in orographic precipitation is included. However, these calculations were performed
574 with a constant I_{up}, whereas changes of infiltration rates are likely to happen in carbonate
575 terrains; depending on the initial stage and evolution of the karst network. High infiltration rates
576 to the karst system will facilitate the growth of internally drained basins in the central parts of the
577 uplifted area due to the long time needed for integration. When dissolution is considered without
578 infiltration, it has the opposite effect of decreasing the response time to external forcing. In our
579 model, this decrease is < 1 Ma. The long response time of streams experiencing infiltration
580 explains the limited fluvial integration of the internal parts of carbonate massifs on Crete and the
581 occurrence of internally drained basins since these areas started uplifting after 10 Ma (van
582 Hinsbergen & Meulenkamp, 2006).
583
584 **6 DISCUSSION**
585 High carbonate massifs on Crete are probably related to a mix of all the effects
586 mentioned above. Some of the ranges are bound by active faults (Fig. 1) and might have
587 exhibited higher uplift rates in the past. For instance, the southern Lefka Ori Mountains are

588 bound by the same active faults as the mountains in western Crete within the PQ unit; however,
589 we do not know if other, now inactive, faults caused higher uplift rates in the Lefka Ori in the
590 Pliocene or Early Pleistocene. Yet, Pleistocene uplift rates along the southwest coast of Crete,
591 show that the mountain ranges PQ mountain ranges in western Crete and the Lefka Ori carbonate
592 massif experience uniform coastal uplift rates (Ott et al., 2019) while exhibiting >1.5 km more
593 relief in the carbonates. As these carbonate mountain ranges started uplifting, substantial
594 infiltration of up to 90% of surface runoff increased the response time to tectonic forcing and
595 fostered the establishment of internally drained basins in the center of the massifs. Internally
596 drained basins such as the Lassithi Plateau are now common within the uplifted Cretan carbonate
597 massifs.

598 Our results imply that in a Mediterranean climate, mechanical rock removal is
599 responsible for more than half of the surface lowering and that uplift above the groundwater
600 table induces infiltration that needs to be compensated by steepening topography. This
601 explanation provides a mechanism for why carbonate areas in the Mediterranean typically
602 exhibit high local relief and areas with different tectonic and climatic forcing such as the
603 Appalachian Mountains in the US or southern Ireland and England comprise low relief carbonate
604 topography (Gallen, 2018; Mills, 2003; Simms, 2004). Carbonates in regions with high localized
605 uplift and unfavorable conditions for dissolution will respond to the uplift forcing mainly by
606 mechanical rock removal that will require more steepening as the topography is elevated above
607 the groundwater table. In contrast, areas of lower uplift and conditions more favorable for
608 dissolution, rock uplift will be balanced mostly by dissolution. Steep slopes are not required for
609 steady-state in such conditions (U minus D close to zero and therefore low k_{sd} value).

610 Variable dissolution and hydrology along stream profiles as they occur in carbonate
611 settings are parameters that could be implemented into landscape evolution models. By
612 constraining the hydrology and dissolution behavior of a study area, landscape evolution models
613 and river profile analysis could be used to extract information such as tectonic and climatic
614 forcings from otherwise hard to analyze karstic terrains. On Crete, the limited number of karst
615 springs suggests that a substantial fraction of the infiltrated water leaves through groundwater
616 submerged springs into the sea. However, in some areas on Crete and many worldwide
617 groundwater daylights in large karst springs. These sudden changes of discharge along a river
618 profile are another mechanism that will greatly influence the shape of stream profiles and show
619 the importance of characterizing the hydrologic behavior of a karst system before analyzing the
620 topography.

621 **7 CONCLUSIONS**

622 We present new water chemistry and detrital ^{36}Cl-denudation data from Crete to partition
623 the total denudation in carbonate catchments between chemical dissolution and mechanical
624 erosion. Water chemistry data show that on Crete, $[Ca^{2+}]$ and $[Mg^{2+}]$ decrease with elevation and
625 are lower for aquifer water derived from high elevation massifs due to less vegetation and higher
626 infiltration rates. An increase in runoff with altitude slightly offsets this decrease in dissolution
627 rates resulting in a more moderate decrease with elevation. These carbonate dissolution rates
628 account for ~ 40% of the total surface lowering of 0.13 mm/a, as measured with ^{36}Cl in
629 carbonate catchments on Crete. The remainder is accomplished through mechanical rock
630 removal as implied by the correlation of k_{sn}, relief and elevation with total denudation rate. In
631 meta-clastic catchments denudation rates were similar (~0.1 mm/a) with less than 10% of
632 chemical rock removal.

Our numerical model of carbonate denudation showed that there are distinct differences between siliciclastic or metamorphic bed channels and carbonate bed channels that are affected by both water infiltration into karstic features and dissolution of bedrock. Dissolution affects river profiles through chemical lowering of channel beds. Changes in dissolution rate with elevation, thus alter the shape of river profiles by changing the channel steepness. In contrast, the infiltration of runoff to groundwater in karstic areas will increase the maximum elevation and relief of a landscape. The infiltration in karst areas will increase the response time to external forcing and facilitate the establishment of internally drained basins in the center of an uplifted block, whereas dissolution will decrease the response time of a landscape. This interpretation implies that high and steep carbonate topography in the Mediterranean is likely related to high local uplift rates, where dissolution is not able to balance uplift, and mechanical rock removal requires steep slopes as runoff is mostly lost to the subsurface.

ACKNOWLEDGMENTS

Acknowledgment is made to the Subitop training network as part of the Marie Curie programme, grant number 674899. We thank the National Water Monitoring Network, Greece for providing water chemistry data. JKCR is funded by an ETH Fellowship. We would like to acknowledge the help of Negar Haghipour in preparing the ^{10}Be samples. We thank M. Covington, S. Marrero and an anonymous reviewer for their constructive reviews that helped to improve this manuscript. We thank A. Bufe for providing a code to calculate the pCO_2 of samples supersaturated in respect to calcite. The authors declare that the data supporting the findings of this study are available within the paper and its supplementary material.

References

Ford, T. D., & Cullingford, C. H.D. (Eds.). (1976). *The Science of Speleology*. *The erosion of limestones*. Academic Press, London, pp. 151-171.

Bickle, M. J., Tipper, E., Galy, A., Chapman, H., & Harris, N. (2015). On discrimination between carbonate and silicate inputs to Himalayan rivers. *American Journal of Science*, *315*(2), 120–166. https://doi.org/10.2475/02.2015.02

Bierman, P. R., Caffee, M. W., Davis, P. T., Marsella, K., Pavich, M., Colgan, P., . . . Larsen, J. (2002). Rates and Timing of Earth Surface Processes From In Situ-Produced Cosmogenic Be-10. *Reviews in Mineralogy and Geochemistry*, *50*(1), 147–205. https://doi.org/10.2138/rmg.2002.50.4

Bohn, U., & Gollub, G. (2000). *Karte der natürlichen Vegetation Europas: = Map of the natural vegetation of Europe*. Münster: BfN-Schriftenvertrieb im Landwirtschaftsverl.

Braucher, R., Merchel, S., Borgomano, J., & Bourlès, D. L. (2011). Production of cosmogenic radionuclides at great depth: A multi element approach. *Earth and Planetary Science Letters*, *309*(1-2), 1–9. https://doi.org/10.1016/j.epsl.2011.06.036

Brook, G. A., & Box, E. O. (1984). A world model of soil carbon dioxide: A reply. *Earth Surface Processes and Landforms*, *9*(1), 85–87. https://doi.org/10.1002/esp.3290090110

Brook, G. A., Folkoff, M. E., & Box, E. O. (1983). A world model of soil carbon dioxide. *Earth Surface Processes and Landforms*, *8*(1), 79–88. https://doi.org/10.1002/esp.3290080108

Brown, E. T., Stallard, R. F., Larsen, M. C., Raisbeck, G. M., & Yiou, F. (1995). Denudation rates determined from the accumulation of in situ-produced 10Be in the luquillo experimental forest, Puerto Rico. *Earth and Planetary Science Letters*, *129*(1-4), 193–202. https://doi.org/10.1016/0012-821X(94)00249-X

679 Calmels, D., Gaillardet, J., & François, L. (2014). Sensitivity of carbonate weathering to soil CO
680 2 production by biological activity along a temperate climate transect. *Chemical Geology*,
681 *390*, 74–86. https://doi.org/10.1016/j.chemgeo.2014.10.010
682 Caputo, R., Catalano, S., Monaco, C., Romagnoli, G., Tortorici, G., & Tortorici, L. (2010).
683 Active faulting on the island of Crete (Greece). *Geophysical Journal International*, *183*, 111–
684 126. https://doi.org/10.1111/j.1365-246X.2010.04749.x
685 Christl, M., Vockenhuber, C., Kubik, P. W., Wacker, L., Lachner, J., Alfimov, V., & Synal, H.-
686 A. (2013). The ETH Zurich AMS facilities: Performance parameters and reference materials.
687 *Nuclear Instruments and Methods in Physics Research Section B: Beam Interactions with*
688 *Materials and Atoms*, *294*, 29–38. https://doi.org/10.1016/j.nimb.2012.03.004
689 Cotton, J. M., & Sheldon, N. D. (2012). New constraints on using paleosols to reconstruct
690 atmospheric pCO2. *Geological Society of America Bulletin*, *124*(9-10), 1411–1423.
691 https://doi.org/10.1130/B30607.1
692 Covington, M. D., Prelovšek, M., & Gabrovšek, F. (2013). Influence of CO2 dynamics on the
693 longitudinal variation of incision rates in soluble bedrock channels: Feedback mechanisms.
694 *Geomorphology*, *186*, 85–95. https://doi.org/10.1016/j.geomorph.2012.12.025
695 Creutzburg, N. (1977). *General Geological Map of Greece: Crete Island, 1: 200 000*: Institute of
696 Geology and Mining Research.
697 Daubenmire, R. F. (1943). Vegetational Zonation in the Rocky Mountains. *Botanical Review*, *9*,
698 325–393.
699 Dixon, J. L., & Blanckenburg, F. von (2012). Soils as pacemakers and limiters of global silicate
700 weathering. *Comptes Rendus Geoscience*, *344*(11-12), 597–609.
701 https://doi.org/10.1016/j.crte.2012.10.012

Driscoll, F. G. (1987). *Groundwater and wells: A comprehensive study of groundwater and the technologies used to locate, extract, treat, and protect this resource* (2. ed.). St. Paul, Minn.: Johnson.

Fabel, D., Henricksen, D., Finlayson, B. L., & Webb, J. A. (1996). Nickpoint recession in Karst terrains: An example from the Buchan karst, Southeastern Australia. *Earth Surface Processes and Landforms*, *21*(5), 453–466. https://doi.org/10.1002/(SICI)1096-9837(199605)21:5<453::AID-ESP608>3.0.CO;2-4

Fassoulas, C., Kilias, A., & Mountrakis, D. (1994). Postnappe stacking extension and exhumation of high-pressure/low-temperature rocks in the island of Crete, Greece. *Tectonics*, *13*(1), 127–138. https://doi.org/10.1029/93TC01955

Fick, S. E., & Hijmans, R. J. (2017). WorldClim 2: New 1-km spatial resolution climate surfaces for global land areas. *International Journal of Climatology*, *37*(12), 4302–4315. https://doi.org/10.1002/joc.5086

Flint, J. J. (1974). Stream gradient as a function of order, magnitude, and discharge. *Water Resources Research*, *10*(5), 969–973. https://doi.org/10.1029/WR010i005p00969

Frumkin, A. (2013). 6.1 New Developments of Karst Geomorphology Concepts. *00808852*.

Gaillardet, J., Dupré, B., Louvat, P., & Allègre, C. J. (1999). Global silicate weathering and CO2 consumption rates deduced from the chemistry of large rivers. *Chemical Geology*, *159*(1-4), 3–30. https://doi.org/10.1016/S0009-2541(99)00031-5

Gaillardet, J., Calmels, D., Romero-Mujalli, G., Zakharova, E., & Hartmann, J. (2018). Global climate control on carbonate weathering intensity. *Chemical Geology.* Advance online publication. https://doi.org/10.1016/j.chemgeo.2018.05.009

Gallen, S. F., Wegmann, K. W., Bohnenstiehl, D. R., Pazzaglia, F. J., Brandon, M. T., & Fassoulas, C. (2014). Active simultaneous uplift and margin-normal extension in a forearc high, Crete, Greece. *Earth and Planetary Science Letters*, *398*, 11–24. https://doi.org/10.1016/j.epsl.2014.04.038

Gallen, S. F. (2018). Lithologic controls on landscape dynamics and aquatic species evolution in post-orogenic mountains. *Earth and Planetary Science Letters*, *493*, 150–160. https://doi.org/10.1016/j.epsl.2018.04.029

Gallen, S. F., & Wegmann, K. W. (2017). River profile response to normal fault growth and linkage: an example from the Hellenic forearc of south-central Crete, Greece. *Earth Surface Dynamics*, *5*(1), 161–186. https://doi.org/10.5194/esurf-5-161-2017

Godard, V., Ollivier, V., Bellier, O., Miramont, C., Shabanian, E., Fleury, J., . . . Guillou, V. (2016). Weathering-limited hillslope evolution in carbonate landscapes. *Earth and Planetary Science Letters*, *446*, 10–20. https://doi.org/10.1016/j.epsl.2016.04.017

Godsey, S. E., Kirchner, J. W., & Clow, D. W. (2009). Concentration-discharge relationships reflect chemostatic characteristics of US catchments. *Hydrological Processes*, *23*(13), 1844–1864. https://doi.org/10.1002/hyp.7315

Gombert, P. (2002). Role of karstic dissolution in global carbon cycle. *Global and Planetary Change*, *33*(1-2), 177–184. https://doi.org/10.1016/S0921-8181(02)00069-3

Goodchild, J. G. (1890). VIII.—Notes on some Observed Rates of Weathering of Limestones. *Geological Magazine*, *7*, 463–466.

Gunn, J. (1981). Limestone solution rates and processes in the Waitomo District, New Zealand. *Earth Surface Processes and Landforms*, *6*(5), 427–445. https://doi.org/10.1002/esp.3290060504

747 Helman, D., Givati, A., & Lensky, I. M. (2015). Annual evapotranspiration retrieved from
748 satellite vegetation indices for the eastern Mediterranean at 250 m spatial resolution.
749 *Atmospheric Chemistry and Physics*, *15*(21), 12567–12579. https://doi.org/10.5194/acp-15-
750 12567-2015
751 Hijmans, R. J., Cameron, S. E., Parra, J. L., Jones, P. G., & Jarvis, A. (2005). Very high
752 resolution interpolated climate surfaces for global land areas. *International Journal of*
753 *Climatology*, *25*(15), 1965–1978. https://doi.org/10.1002/joc.1276
754 Howard, A. d. (1994). A detachment-limited model of drainage basin evolution. *Water*
755 *Resources Research*, *30*(7), 2261–2285. https://doi.org/10.1029/94WR00757
756 Humboldt, A. von. (1806). *Ideen zu einer Physiognomik der Gewächse.*
757 Hutton, J. (1795). *Theory of the earth: With proofs and illustrations*: Library of Alexandria.
758 Ivy-Ochs, S., Synal, H.-A., Roth, C., & Schaller, M. (2004). Initial results from isotope dilution
759 for Cl and 36Cl measurements at the PSI/ETH Zurich AMS facility. *Nuclear Instruments and*
760 *Methods in Physics Research Section B: Beam Interactions with Materials and Atoms*, *223-*
761 *224*, 623–627. https://doi.org/10.1016/j.nimb.2004.04.115
762 Kallianis, G., & Chatzitheodorou, K. (2003). *Hydrological analysis of Kilaris River Basin*
763 (Diploma). Technical University of Crete, Chania.
764 Larsen, I. J., Almond, P. C., Eger, A., Stone, J. O., Montgomery, D. R., & Malcolm, B. (2014).
765 Rapid soil production and weathering in the Southern Alps, New Zealand. *Science (New York,*
766 *N.Y.)*, *343*(6171), 637–640. https://doi.org/10.1126/science.1244908
767 Lupker, M., Blard, P.-H., Lavé, J., France-Lanord, C., Leanni, L., Puchol, N., . . . Bourlès, D.
768 (2012). 10Be-derived Himalayan denudation rates and sediment budgets in the Ganga basin.

769 *Earth and Planetary Science Letters*, *333-334*, 146–156.
770 https://doi.org/10.1016/j.epsl.2012.04.020
771 Malard, A., Sinreich, M., & Jeannin, P.-Y. (2016). A novel approach for estimating karst
772 groundwater recharge in mountainous regions and its application in Switzerland.
773 *Hydrological Processes*, *30*(13), 2153–2166. https://doi.org/10.1002/hyp.10765
774 Marrero, S. M., Phillips, F. M., Borchers, B., Lifton, N., Aumer, R., & Balco, G. (2016).
775 Cosmogenic nuclide systematics and the CRONUScalc program. *Quaternary Geochronology*,
776 *31*, 160–187. https://doi.org/10.1016/j.quageo.2015.09.005
777 Meybeck, M. (1987). Global chemical weathering of surficial rocks estimated from river
778 dissolved loads. *American Journal of Science*, *287*(5), 401–428.
779 https://doi.org/10.2475/ajs.287.5.401
780 Mills, H. H. (2003). Inferring erosional resistance of bedrock units in the east Tennessee
781 mountains from digital elevation data. *Geomorphology*, *55*(1-4), 263–281.
782 https://doi.org/10.1016/S0169-555X(03)00144-2
783 Newson, M. D. (1971). A Model of Subterranean Limestone Erosion in the British Isles Based
784 on Hydrology. *Transactions of the Institute of British Geographers*. (54), 55.
785 https://doi.org/10.2307/621362
786 Nikolaidis, N. P., Bouraoui, F., & Bidoglio, G. (2013). Hydrologic and geochemical modeling of
787 a karstic Mediterranean watershed. *Journal of Hydrology*, *477*, 129–138.
788 https://doi.org/10.1016/j.jhydrol.2012.11.018
789 Ott, R. F., Gallen, S. F., Wegmann, K. W., Biswas, R. H., Herman, F., & Willett, S. D. (2019).
790 Pleistocene terrace formation, Quaternary rock uplift rates and geodynamics of the Hellenic

Subduction Zone revealed from dating of paleoshorelines on Crete, Greece. *Earth and Planetary Science Letters*, *525*, 115757. https://doi.org/10.1016/j.epsl.2019.115757

Palmer, A. N. (1991). Origin and morphology of limestone caves. *Geological Society of America Bulletin*, *103*(1), 1–21. https://doi.org/10.1130/0016-7606(1991)103<0001:OAMOLC>2.3.CO;2

Papaioannou, A. (2007). *Chemical Analyses in Table Waters* (Diploma). Technical University of Crete, Chania.

Parkhurst, D. L., & Appelo, C. A.J. (1999). User's guide to PHREEQC (Version 2): A computer program for speciation, batch-reaction, one-dimensional transport, and inverse geochemical calculations.

Peterek, A., & Schwarze, J. (2004). Architecture and Late Pliocene to recent evolution of outer-arc basins of the Hellenic subduction zone (south-central Crete, Greece). *Journal of Geodynamics*, *38*, 19–55. https://doi.org/10.1016/j.jog.2004.03.002

Plan, L. (2005). Factors controlling carbonate dissolution rates quantified in a field test in the Austrian alps. *Geomorphology*, *68*(3-4), 201–212. https://doi.org/10.1016/j.geomorph.2004.11.014

Plummer, L.N., & Busenberg, E. (1982). The solubilities of calcite, aragonite and vaterite in CO2-H2O solutions between 0 and 90°C, and an evaluation of the aqueous model for the system CaCO3-CO2-H2O. *Geochimica et Cosmochimica Acta*, *46*(6), 1011–1040. https://doi.org/10.1016/0016-7037(82)90056-4

Polychronaki, A., Pavlidou, S., & Zouridakis, N. (2009). Water Isotopic Analyses: Water Region of Crete, 1–31.

Prager, C., Ivy-Ochs, S., Ostermann, M., Synal, H.-A., & Patzelt, G. (2009). Geology and radiometric 14C-, 36Cl- and Th-/U-dating of the Fernpass rockslide (Tyrol, Austria). *Geomorphology*, *103*(1), 93–103. https://doi.org/10.1016/j.geomorph.2007.10.018

Rahl, J. M., Anderson, K. M., Brandon, M. T., & Fassoulas, C. (2005). Raman spectroscopic carbonaceous material thermometry of low-grade metamorphic rocks: Calibration and application to tectonic exhumation in Crete, Greece. *Earth and Planetary Science Letters*, *240*, 339–354. https://doi.org/10.1016/j.epsl.2005.09.055

Reilinger, R., McClusky, S., Vernant, P., Lawrence, S., Ergintav, S., Cakmak, R., . . . Karam, G. (2006). GPS constraints on continental deformation in the Africa-Arabia-Eurasia continental collision zone and implications for the dynamics of plate interactions. *Journal of Geophysical Research*, *111*, 26. https://doi.org/10.1029/2005JB004051

Ryb, U., Matmon, A., Erel, Y., Haviv, I., Katz, A., Starinsky, A., . . . Team, A. (2014). Controls on denudation rates in tectonically stable Mediterranean carbonate terrain. *GSA Bulletin*, *126*(3-4), 553–568. https://doi.org/10.1130/B30886.1

Schaller, M., Hovius, N., Willett, S. d., Ivy-Ochs, S., Synal, H.-A., & Chen, M.-C. (2005). Fluvial bedrock incision in the active mountain belt of Taiwan fromin situ-produced cosmogenic nuclides. *Earth Surface Processes and Landforms*, *30*(8), 955–971. https://doi.org/10.1002/esp.1256

Schimmelpfennig, I., Benedetti, L., Finkel, R., Pik, R., Blard, P.-H., Bourles, D., . . . Williams, A. (2009). Sources of in-situ 36Cl in basaltic rocks. Implications for calibration of production rates. *Quaternary Geochronology*, *4*(6), 441–461. https://doi.org/10.1016/j.quageo.2009.06.003

Seidel, E., Kreuzer, H., & Harre, W. (1982). A Late Oligocane/early Miocene pressure belt in the External Hellenides. *Geologisches Jahruch. Reihe E: Geophyik*, *23*, 165–206.

Simms, M. J. (2004). Tortoises and hares: dissolution, erosion and isostasy in landscape evolution. *Earth Surface Processes and Landforms*, *29*(4), 477–494. https://doi.org/10.1002/esp.1047

Spring, W., & Prost, E. (1884). Etude sur les eaux de la Meuse: Détermination des quantités de matières diverses roulées par les eaux de ce fleuve pendant l'espace d'une année. *Annales de la Société Géologique de Belgique. Mémoires*, *11*.

Springer, G. S., Wohl, E. E., Foster, J. A., & Boyer, D. G. (2003). Testing for reach-scale adjustments of hydraulic variables to soluble and insoluble strata: Buckeye Creek and Greenbrier River, West Virginia. *Geomorphology*, *56*(1-2), 201–217. https://doi.org/10.1016/S0169-555X(03)00079-5

Stallard, R. F., & Edmond, J. M. (1981). Geochemistry of the Amazon: 1. Precipitation chemistry and the marine contribution to the dissolved load at the time of peak discharge. *J. Geophys. Res.*, *86*(C10), 9844. https://doi.org/10.1029/JC086iC10p09844

Stone, J., Allan, G. L., Fifield, L. K., Evans, J. M., & Chivas, A. R. (1994). Limestone erosion measurements with cosmogenic chlorine-36 in calcite — preliminary results from Australia. *Nuclear Instruments and Methods in Physics Research Section B: Beam Interactions with Materials and Atoms*, *92*(1-4), 311–316. https://doi.org/10.1016/0168-583X(94)96025-9

Stone, J. O. (2000). Air pressure and cosmogenic isotope production. *Journal of Geophysical Research: Solid Earth*, *105*(B10), 23753–23759. https://doi.org/10.1029/2000JB900181

Thomas, F., Godard, V., Bellier, O., Benedetti, L., Ollivier, V., Rizza, M., . . . Keddadouche, K. (2018). Limited influence of climatic gradients on the denudation of a Mediterranean

carbonate landscape. *Geomorphology*, *316*, 44–58. https://doi.org/10.1016/j.geomorph.2018.04.014

Van Hinsbergen, Douwe Jacob Jan, Hafkenscheid, E., Spakman, W., Meulenkamp, J. E., & Wortel, R. (2005). Nappe stacking resulting from subduction of oceanic and continental lithosphere below Greece. *Geology*, *33*, 325–328. https://doi.org/10.1130/g20878.1

Van Hinsbergen, D. J., & Meulenkamp, J. E. (2006). Neogene supradetachment basin development on Crete (Greece) during exhumation of the South Aegean core complex. *Basin Research*, *18*(1), 103–124. https://doi.org/10.1111/j.1365-2117.2005.00282.x

Vockenhuber, C., Miltenberger, K.-U., & Synal, H.-A. (2019). 36Cl measurements with a gas-filled magnet at 6 MV. *Nuclear Instruments and Methods in Physics Research Section B: Beam Interactions with Materials and Atoms.* Advance online publication. https://doi.org/10.1016/j.nimb.2018.12.046

Wegmann, K. W. (2008). *Tectonic geomorphology above Mediterranean subduction zones; northern Apennines of Italy and Crete, Greece.* Lehigh University, Bethlehem, PA.

Whipple, K. X., Hancock, G. S., & Anderson, R. S. (2000). River incision into bedrock: Mechanics and relative efficacy of plucking, abrasion, and cavitation. *Geology*, *112*(3), 490–503. https://doi.org/10.1130/0016-7606(2000)112<490:RIIBMA>2.0.CO;2

Whipple, K. X., & Tucker, G. E. (1999). Dynamics of the stream-power river incision model: Implications for height limits of mountain ranges, landscape response timescales, and research needs. *Journal of Geophysical Research: Solid Earth*, *104*(B8), 17661–17674. https://doi.org/10.1029/1999JB900120

White, W. B. (1984). *Rate processes: chemical kinetics and karst landform development*: Allen & Unwin Incorporated.

Woodside, J., Peterson, E., & Dogwiler, T. (2015). Longitudinal profile and sediment mobility as geomorphic tools to interpret the history of a fluviokarst stream system. *International Journal of Speleology*, *44*(2), 197–206. https://doi.org/10.5038/1827-806X.44.2.9

Xu, S., Liu, C., Freeman, S., Lang, Y., Schnabel, C., Tu, C., . . . Zhao, Z. (2013). In-situ cosmogenic 36Cl denudation rates of carbonates in Guizhou karst area. *Chinese Science Bulletin*, *58*(20), 2473–2479. https://doi.org/10.1007/s11434-013-5756-8

Zachariasse, W. J., van Hinsbergen, D.J.J., & Fortuin, A. R. (2008). Mass wasting and uplift on Crete and Karpathos during the early Pliocene related to initiation of south Aegean left-lateral, strike-slip tectonics. *Geological Society of America Bulletin*, *120*, 976–993. https://doi.org/10.1130/b26175.1

8 FIGURE CAPTIONS

Figure 1: (a) Topography of Crete and sampling sites for cosmogenic nuclides and water. The rectangle depicts the locations of the close-ups in figure 4. Inset: Location of Crete within the Mediterranean. (b) Simplified geologic map of Crete after Creutzburg (1977) with faults and outlines of sampled basins for catchment average denudation rates. (c) Cumulative hypsometric curve of the main lithologies on Crete. The colors for lithologic units in (b) and (c) are identical. Note that carbonate lithologies are disproportionately over-represented at high elevations.

Figure 2: Typical appearance of the high elevation areas within the carbonate massifs (a) and meta-clastic PQ catchments (b) on Crete.

Figure 3: Schematic diagram of the steps involved in the carbonate dissolution rate calculation.

Figure 4: Catchment average denudation rates from cosmogenic nuclides. Catchments with dominantly PQ bedrock where ^{10}Be was measured are outlined in black, ^{36}Cl carbonate catchments in red. The locations for (a), (b) and (c) are indicated in figure 1a. The catchment labels correspond to the numbers in Tab. 1.

Figure 5: Correlation between denudation rates and catchment metrics. (a – f). Local relief was calculated with a 500 m radius on a 30m Shuttle Radar Topography Mission (SRTM) digital elevation model (DEM).Regression lines and their correlation coefficients are shown in black for ^{10}Be catchments and red for ^{36}Cl catchments. (g) Matrix of correlation coefficients within the dataset (HI – Hypsometric Index). The upper triangle with the black outline corresponds to data from the ^{36}Cl catchments. The lower triangle shows data from the ^{10}Be catchments. The catchment metrics are listed on the sides and the correlation coefficients are colored by their respective value. All correlation coefficients were calculated with uncertainties reported in the methods section. A matrix of p-values for this table is provided in the supplement (Tab. S7).

Figure 6: Boxplots of $[Ca^{2+}]$ (a), $[Mg^{2+}]$ (b) concentrations and $\log_{10}(pCO_2)$ for different types of water sources with boxes representing 25% and 75% percentiles and the mean (red bar) (all n = 15; river n = 6, drill n = 4, spring n = 5). For locations with time-series, only one-time averaged value was incorporated. The dark grey boxes include the theoretical pCO_2 at which

926 samples oversaturated with respect to calcite would have been in equilibrium prior to degassing.
927 We calculated the theoretical pCO_2 values for supersaturated samples by adding acidity from
928 CO_2 until saturation is achieved. Subsequently, the new pH estimate of the solution is used in
929 PhreeQC with all other inputs held equal to calculate the pCO_2 prior to degassing.
930
931 Figure 7: Calcium concentration (a), calcite saturation index (b) and calculated carbonate
932 dissolution rate (c) against the mean elevation of the estimated recharge area with 1 σ error bars.
933
934 Figure 8: Total denudation rates from ^{36}Cl measurements against local relief with
935 regression line (red line) and correlation coefficient. Blue circles depict carbonate dissolution
936 rates calculated from water data. We interpret the difference between the two rates as the effect
937 of mechanical weathering within the carbonate catchments.
938
939 Figure 9: Carbonate denudation model. (a) Steady state elevations of river profiles for 4
940 different denudation process combinations. SPM – stream power model incision. (b) Rates of
941 different input parameters for the SPM & infiltration & dissolution model run. P, AET and soil
942 CO_2 are empirical functions of altitude and therefore change along the model domain with the
943 uplifting topography. (c) Rates of total, mechanical denudation and dissolution of the same
944 model as in (b). (d) Dissolution channel steepness index k_{sd} for the SPM model, a model with the
945 calculated dissolution rate and a model using the regression line equation from figure 7c as
946 dissolution-scaling. Note, stream profiles without dissolution will have a constant k_s value along
947 stream, while stream profiles with altitude dependent dissolution will change their channel
948 steepness along profile.

Table 1: Cosmogenic nuclide samples, AMS concentrations and derived denudation rates.

#	Lab ID	Latitude	Longitude	catchment area	mean elevation			[^{10}Be]	Erosion rate
		°N	°E	km²	m			10^4 atoms/g	[mm/a]
1	WC-616-2	35.4298	23.924	14.1	333.8			3.72 ± 0.32	0.088 ± 0.013
2	WC-616-3	35.4518	23.7903	21.6	612.7			2.63 ± 0.23	0.154 ± 0.020
3	WC-616-4	35.4515	23.7864	28.1	560.8			4.35 ± 0.18	0.090 ± 0.010
4	WC-616-5	35.4054	23.6829	30.9	576.3			8.04 ± 0.33	0.049 ± 0.005
5	WC-616-6	35.4056	23.7094	15.4	543.3			3.33 ± 0.26	0.115 ± 0.015
6	WC-616-7	35.3297	23.5582	34.7	577.9			3.78 ± 0.24	0.104 ± 0.013
7	WC-616-9	35.4166	23.5698	9.8	490.2			4.38 ± 0.28	0.084 ± 0.010
8	WC-616-10	35.273	23.6664	18.6	570.3			4.71 ± 0.23	0.083 ± 0.010
9	WC-616-11	35.2599	23.6022	14.4	497.3			6.88 ± 0.42	0.059 ± 0.010
10	WC-616-12	35.2735	23.6606	34.2	638.4			5.70 ± 0.26	0.072 ± 0.008
11	WC-616-13	35.2708	23.6853	70.9	576.2			6.32 ± 0.28	0.063 ± 0.008
12	WC-616-14	35.2861	23.8176	20.5	637.5			1.59 ± 0.14	0.262 ± 0.035
13	WC-916-15	35.4633	23.8323	51.4	590.2			4.07 ± 0.19	0.099 ± 0.013
14	WC-617-16	35.1635	24.4742	123.3	490.3			2.90 ± 0.43	0.128 ± 0.023
	Sample	**Latitude**	**Longitude**	**catchment area**	**mean elevation**	**[CaO]**	**[Cl]**	**[^{36}Cl]**	**Erosion rate**
		°N	**°E**	**km²**	**m**	**%**	**ppm**	**10^5 atoms/g**	**[mm/a]**
15	Cl-617-2	35.342	25.6565	8.9	481.3	47.4	90.96	3.59 ± 0.26	0.109 ± 0.014
16	Cl-617-3	35.3333	25.6213	16.1	453.0	48.8	8.17	4.89 ± 0.28	0.052 ± 0.007
17	Cl-617-6	35.2787	24.8296	57.2	1408.7	50.3	3.98	3.60 ± 0.17	0.141 ± 0.016

18	Cl-617-8	35.377	24.1351	24.1	1213.2	37.1	205.66	5.83 ± 0.80	0.16 ± 0.041
19	Cl-617-10	35.3764	24.201	87.4	727.2	48.5	79.87	3.31 ± 0.21	0.128 ± 0.016
20	Cl-617-15	35.1975	24.0572	26.3	1061.6	38.9	168.06	4.74 ± 0.44	0.175 ± 0.031
21	WC-616-8	35.2707	23.9638	38.4	1213.0	50.0	51.48	0.99 ± 0.23	0.556 ± 0.068

Tab. 2: Chemical weathering contribution to the total denudation in the Topolia meta-clastic catchment from the total dissolved load (TDS). Calculation of annual total and chemical denudational flux for 1 m² in the catchment.

TDS	**P**	**AET**	**Q = P- AET**	**Q in m³**	**Solutional flux**	
mg/l	**mm/a**	**mm/a**	**mm/a**	**m^3/a**	**kg/m^3/a**	
58.16	751	553	198	0.198	0.0115	
			Be rate	**Rock density**	**Total flux**	**% Chemical**
			mm/a	**kg/m^3**	**kg/m^3/a**	
			0.049	2700	0.1323	8.71

Figure 1

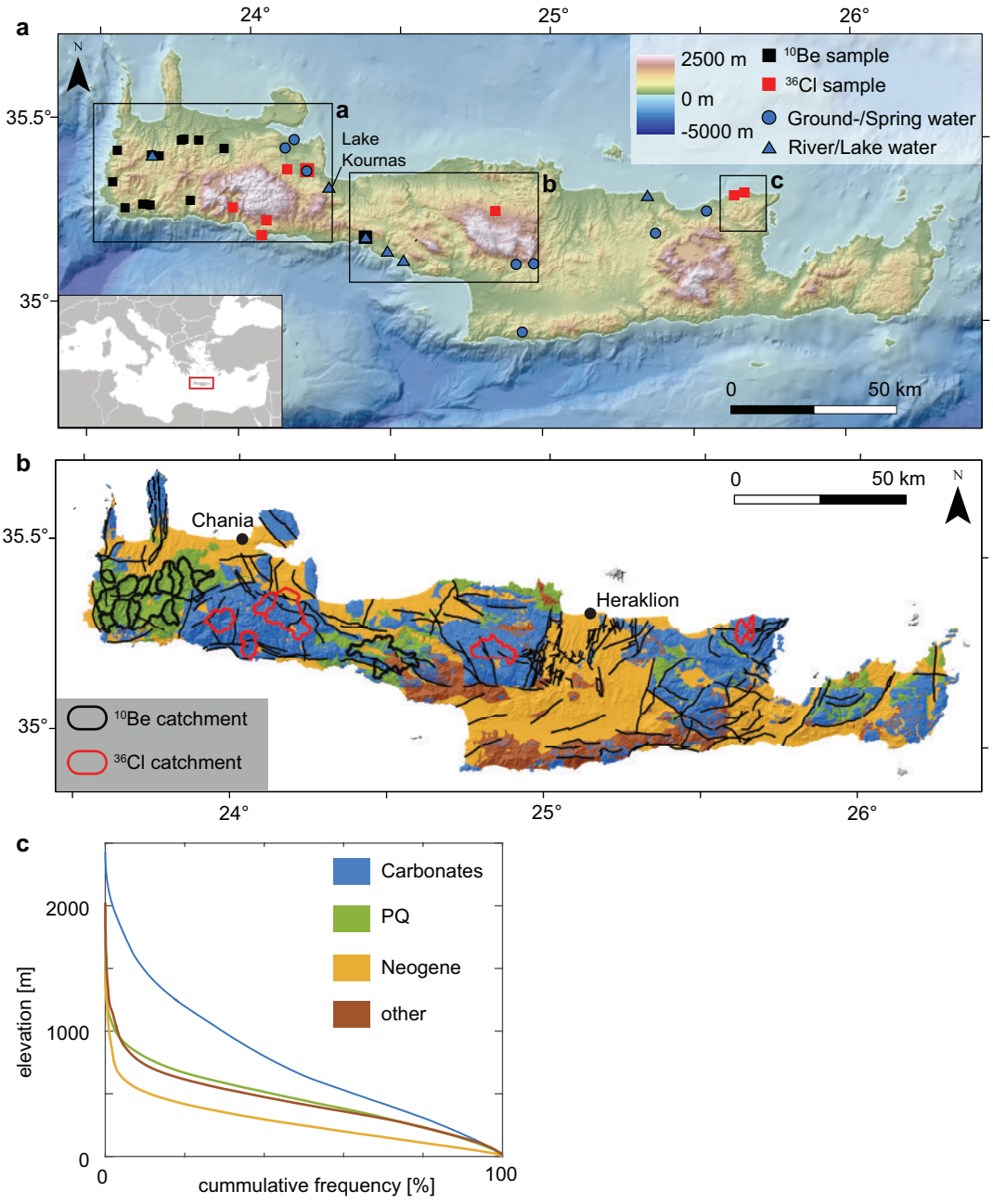
a
24°
25°
26°
35.5°
35°
N
2500 m
0 m
-5000 m
10Be sample
36Cl sample
Ground-/Spring water
River/Lake water
Lake
Kournas
a
b
c
0
50 km
b
35.5°
35°
Chania
Heraklion
0
50 km
N
10Be catchment
36Cl catchment
24°
25°
26°
c
2000
1000
0
elevation [m]
0
100
cummulative frequency [%]
Carbonates
PQ
Neogene
other

Figure 2

Figure 3

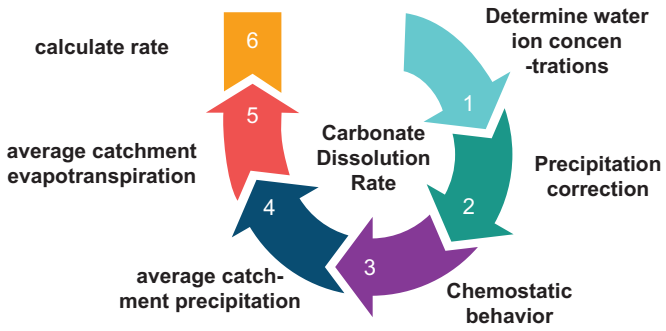
calculate rate
6
Determine water ion concen -trations
1
5
Carbonate Dissolution Rate
Precipitation correction
2
average catchment evapotranspiration
4
3
average catch- ment precipitation
Chemostatic behavior

Figure 4

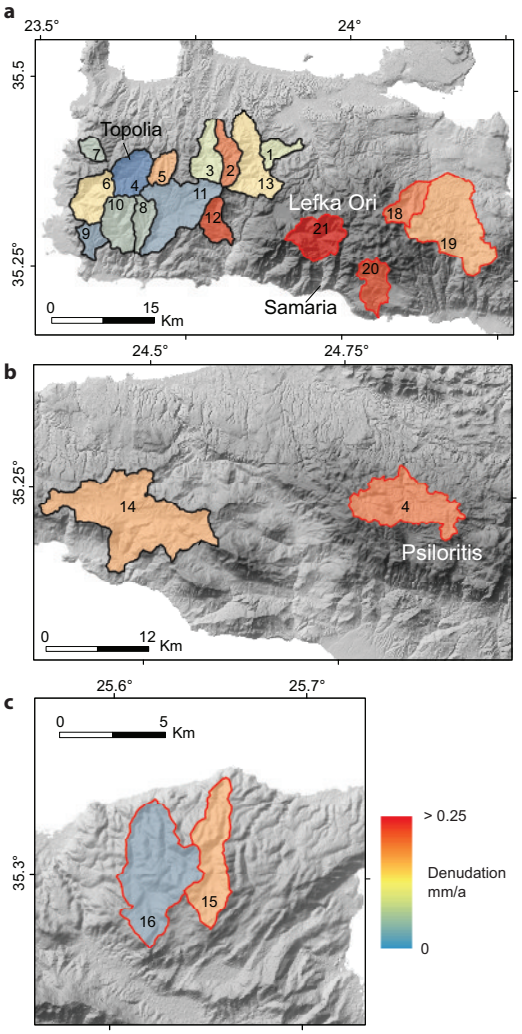
a
23.5°
24°
35.5
35.25°
Topolia
Lefka Ori
Samaria
1
2
3
4
5
6
7
8
9
10
11
12
13
18
19
20
21
0
15
Km
b
24.5°
24.75°
35.25°
14
4
Psiloritis
0
12
Km
c
25.6°
25.7°
35.3°
0
5
Km
15
16
> 0.25
Denudation
mm/a
0

Figure 5

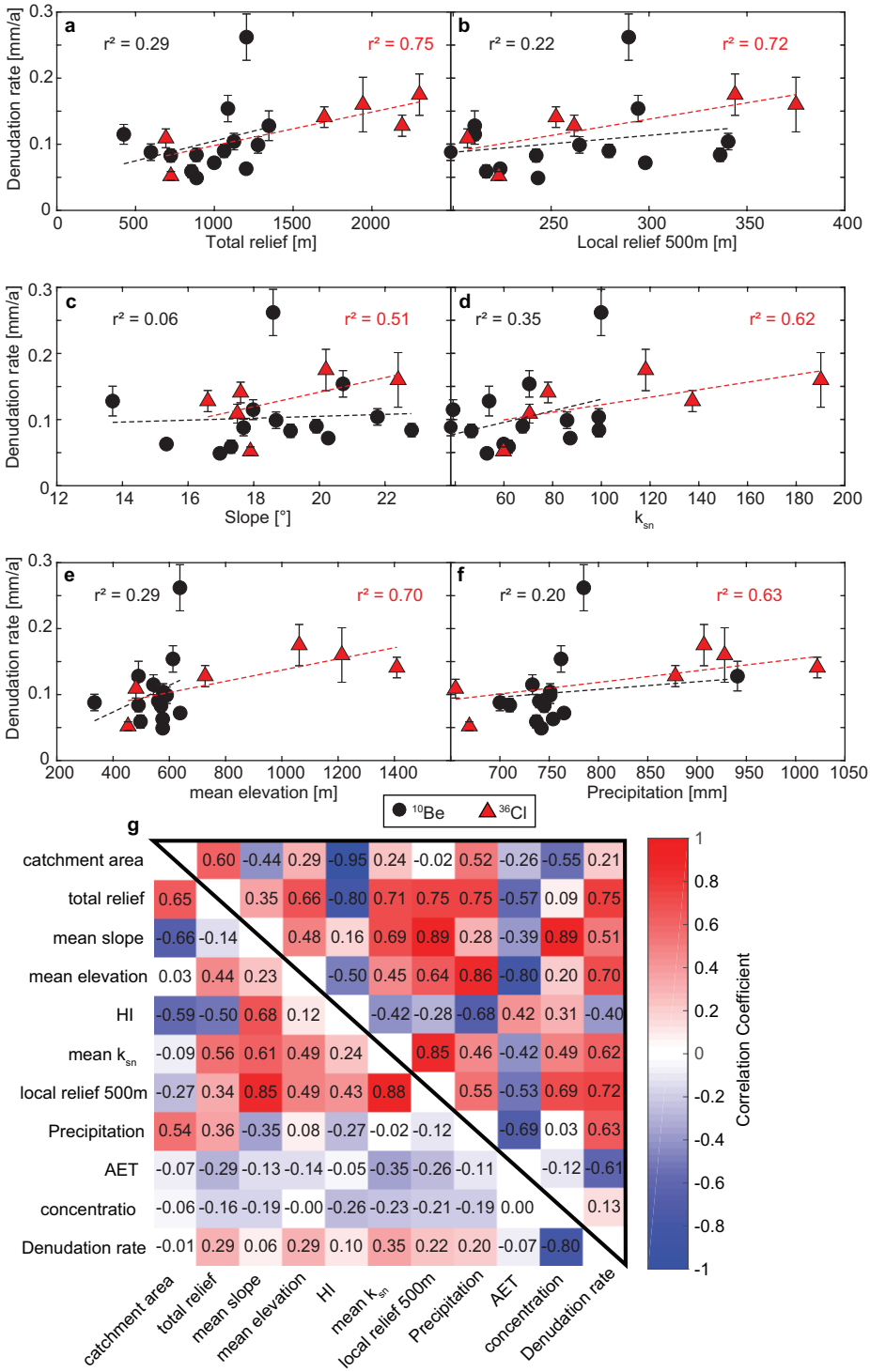
a
r² = 0.29
r² = 0.75
b
r² = 0.22
r² = 0.72
Denudation rate [mm/a]
Total relief [m]
Local relief 500m [m]
c
r² = 0.06
r² = 0.51
d
r² = 0.35
r² = 0.62
Slope [°]
k_sn
e
r² = 0.29
r² = 0.70
f
r² = 0.20
r² = 0.63
mean elevation [m]
Precipitation [mm]
10Be
36Cl
g
catchment area
total relief
mean slope
mean elevation
HI
mean k_sn
local relief 500m
Precipitation
AET
concentratio
Denudation rate
Correlation Coefficient

Figure 6

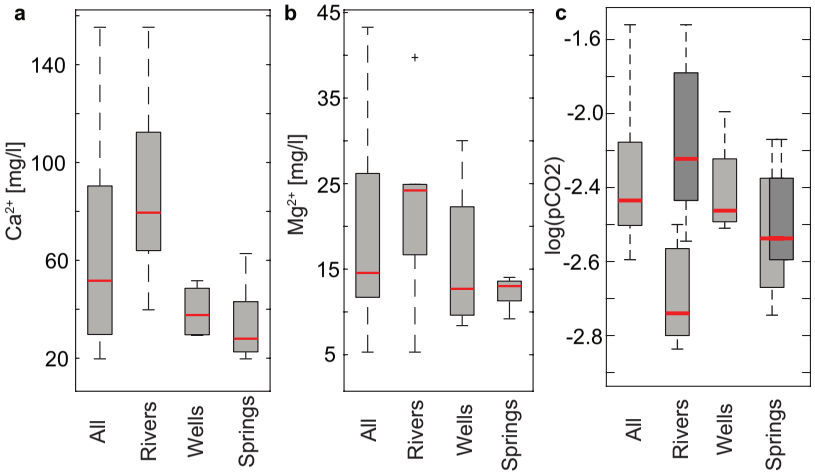
a
b
c
Ca2+ [mg/l]
Mg2+ [mg/l]
log(pCO2)
140
100
60
20
45
35
25
15
5
-1.6
-2.0
-2.4
-2.6
-2.8
All
Rivers
Wells
Springs

Figure 7

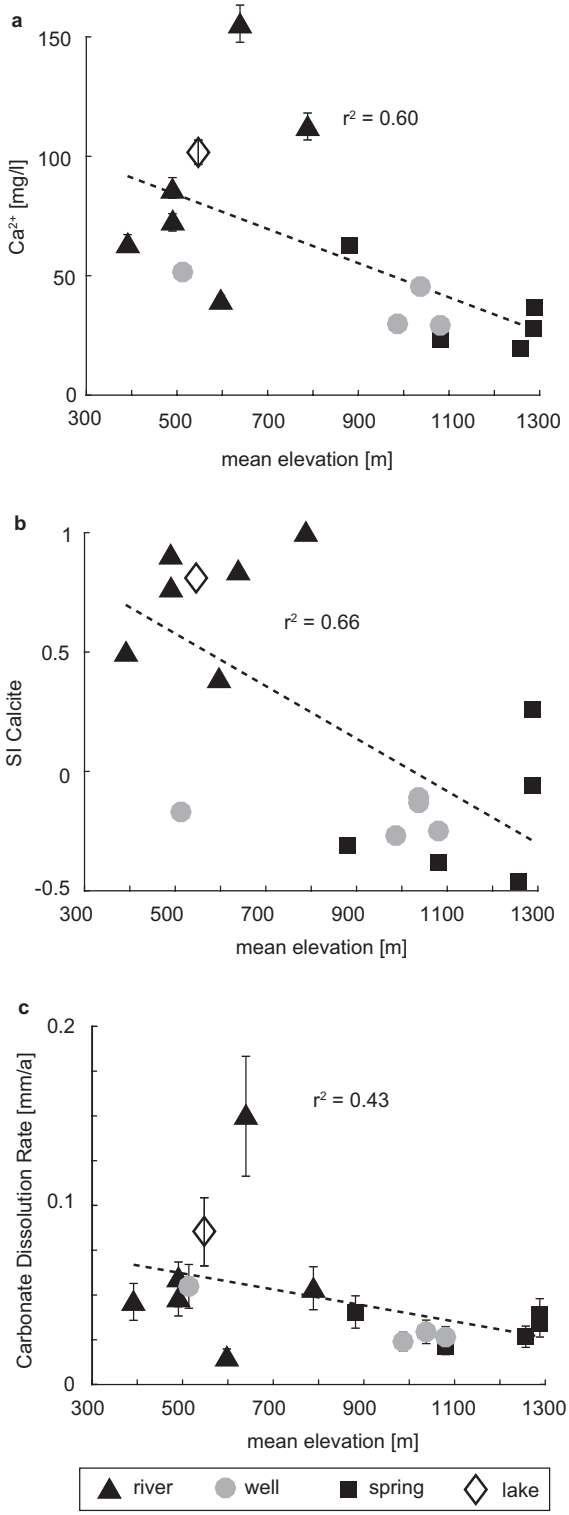
a
150
100
50
0
Ca2+ [mg/l]
r2 = 0.60
300
500
700
900
1100
1300
mean elevation [m]
b
1
0.5
0
-0.5
SI Calcite
r2 = 0.66
300
500
700
900
1100
1300
mean elevation [m]
c
0.2
0.1
0
Carbonate Dissolution Rate [mm/a]
r2 = 0.43
300
500
700
900
1100
1300
mean elevation [m]
river
well
spring
lake

Figure 8

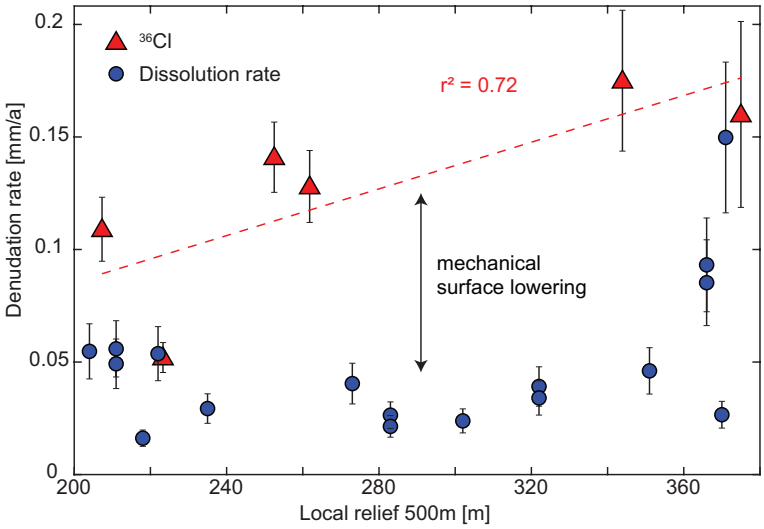
0.2
0.15
0.1
0.05
0
Denudation rate [mm/a]
36Cl
Dissolution rate
r² = 0.72
mechanical
surface lowering
200
240
280
320
360
Local relief 500m [m]

Figure 9

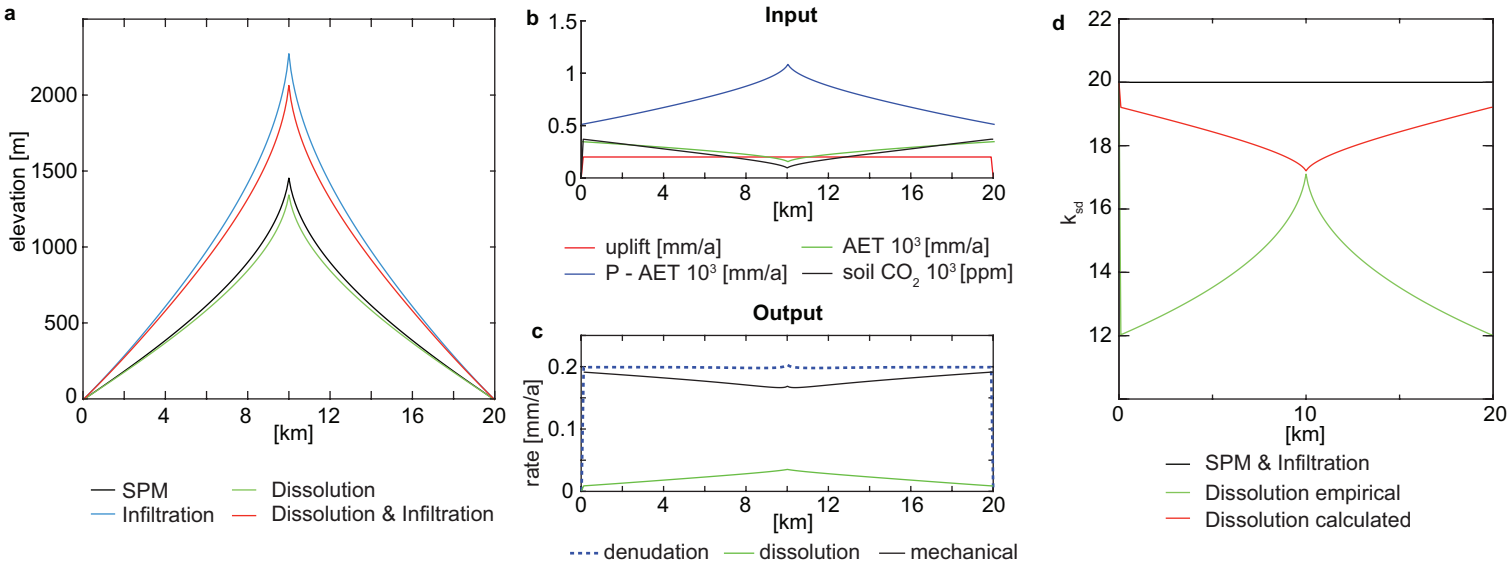
a
elevation [m]
2000
1500
1000
500
0
0
4
8
12
16
20
[km]
SPM
Infiltration
Dissolution
Dissolution & Infiltration
b
Input
1.5
1
0.5
0
0
4
8
12
16
20
[km]
uplift [mm/a]
P - AET 10³ [mm/a]
AET 10³ [mm/a]
soil CO₂ 10³ [ppm]
c
Output
rate [mm/a]
0.2
0.1
0
0
4
8
12
16
20
[km]
denudation
dissolution
mechanical
d
22
20
18
16
14
12
k_sn
0
10
20
[km]
SPM & Infiltration
Dissolution empirical
Dissolution calculated